Kinetic Studies of Fos·Jun·DNA Complex Formation: DNA Binding Prior to Dimerization†

Jennifer J. Kohler and Alanna Schepartz*

Department of Chemistry, Yale University, New Haven, Connecticut 06520-8107

Received August 10, 2000; Revised Manuscript Received October 3, 2000

ABSTRACT: The bZIP proteins Fos and Jun bind DNA rapidly and with high affinity, forming a heteromeric complex that mediates activated transcription. Here we use stopped-flow fluorescence resonance energy transfer (FRET) to study the kinetic pathway by which Fos·Jun·DNA complexes assemble. Though dimerization of Fos and Jun occurs rapidly in the absence of DNA, the rate of dimerization is enhanced in the presence of DNA. Global analysis of the kinetic data shows that the favored DNA binding pathway is one is which the two protein monomers bind DNA sequentially and assemble their dimerization interface while bound to DNA.

Tightly regulated gene expression is essential for normal cellular development and function. Initiation of transcription of any particular gene requires chromatin remodeling and the ordered assembly of the preinitiation complex (PIC),[1] a structure consisting of transcription factors, architectural proteins, and template DNA (*1*, *2*). Many transcriptional activators, key components of the preinitiation complex (*3*−*5*), form dimeric (2:1) complexes with DNA. Dimeric DNA binding proteins are found in a variety of structural families and may exist as either monomers (*6*) or dimers (*7*) in the absence of DNA. Some of the simplest DNA recognition motifs are presented by dimeric transcription factors in the bZIP (*8*), homeodomain (*9*), Rel/NF-κB (*10*), and HLH (*11*) families.

Dimeric DNA binding motifs provide several potential advantages over monomeric motifs. Dimerization offers, through the variance of heterodimeric structures, diversity of both target site recognition and function with minimal genomic investment. For example, a homodimer of the human bHLHZip protein Max specifically recognizes the palindromic Ebox target site. However, Max also has the ability to form heterodimers with other bHLHZip proteins including Myc, Mad3, Mad4, Mxi1, Mnt, and Mitf, the heterodimers often having unique function and DNA binding specificity (*11*−*13*). In this way, a single protein can recognize a number of different target sites and has finely tuned activation potential depending upon the pairing partners available in the cellular context.

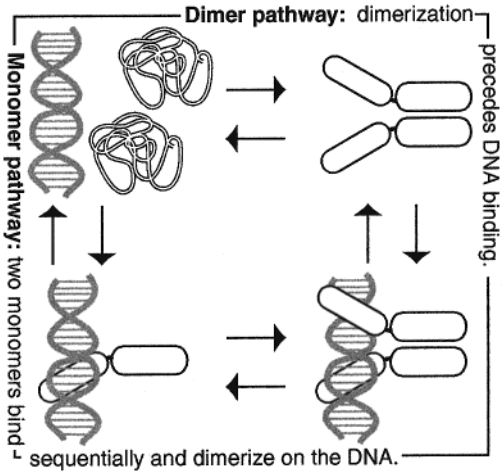

FIGURE 1: Two pathways to describe binding of dimeric proteins to DNA. In the dimer pathway, proteins first form dimers, which then go on to bind DNA. Along the monomer pathway, a monomer·DNA complex is formed first, followed by recruitment of the second monomer to form the final complex.

Dimerization may also offer a kinetic advantage for DNA binding. For proteins that form dimeric complexes with DNA, there exist two limiting pathways that may describe the mechanism of complex assembly (Figure 1) (*14*−*16*). The two monomers can dimerize first, then associate with DNA (dimer pathway), or the two monomers can bind DNA sequentially and assemble their dimerization interface while interacting with DNA (monomer pathway). Since the pathways form a thermodynamic cycle, the equilibrium affinity of the protein for DNA will be equivalent, whether binding proceeds through the monomer pathway, the dimer pathway, or some combination of the two. However, the monomer pathway will often offer a faster route to assembly of the final complex (*15*, *17*, *18*).

A variety of dimeric DNA binding proteins, including the LexA repressor (*14*), ATF-2 (*17*), and Max (*17*), use the

† This work was supported by the NIH (GM 52544). J.J.K. was supported by a NSF graduate research fellowship and by a predoctoral fellowship provided by the American Chemical Society, Division of Medicinal Chemistry.

* To whom correspondence should be addressed. Phone: (203) 432-5094. Fax: (203) 432-3486. E-mail: alanna.schepartz@yale.edu.

[1] Abbreviations: bZIP, basic region leucine zipper; BSA, bovine serum albumin; DNA, deoxyribonucleic acid; DTT, dithiothreitol; EDTA, ethylenediaminetetraacetic acid; FRET, fluorescence resonance energy transfer; HEPES, 4-(2-hydroxyethyl)-1-piperazineethanesulfonic acid; HLH, helix-loop-helix; HPLC, high-performance liquid chromatography; IPTG, 1-thio-β-D-galactopyranoside; MALDI-TOF, matrix-assisted laser desorption−ionization time-of-flight; PEI, polyethyleneimine; PMSF, phenylmethanesulfonyl fluoride; NP-40, Nonidet P-40; NF-κB, nuclear factor kappa-B.

10.1021/bi001881p CCC: $20.00
Published on Web 12/07/2000

monomer pathway. Kinetic experiments with these proteins showed that DNA binding proceeds more rapidly than can be accounted for by the dimer pathway. Evidence of formation of the monomer·DNA intermediate provides further support for the monomer pathway (*14*, *18*). Two main themes emerge from these studies. First, both steps of the monomer pathway are aided by electrostatic interactions between the protein and DNA. Electrostatics can act over large distances to accelerate association rates (*19*). Thus, in many cases, the monomer pathway provides more rapid access to the final complex than would be possible through the dimer pathway whose rate is limited by the rate of protein dimerization (*14*, *17*, *18*, *20*). The effect is likely to be enhanced in cases where folding is coupled to binding. In particular, unfolded proteins (most bZIP monomers) have a greater capture radius than their folded counterparts (most bZIP dimers), thus allowing for an increased rate of molecular recognition (*21*). The second theme is that the monomer·DNA intermediate is generally kinetically unstable relative to the final dimer·DNA complex (*14*, *15*, *18*, *22*). The instability of the intermediate provides a means to discriminate among potential target sites. By binding DNA through the monomer pathway, transcription factors can rapidly search for specific DNA target sites without becoming kinetically trapped at nonspecific sites (*17*, *23*).

We were interested in investigating the generality of the monomer binding pathway. We chose to extend our studies of the mechanism of transcription factor binding by considering the bZIP elements of the proteins cFos and cJun. Together, cFos and cJun form the heterodimeric transcription factor AP-1, which activates transcription of variety of genes (reviewed in refs *24*−*27*). Consideration of Fos and Jun extends our investigations of dimeric transcription factors in two ways. First, the Fos·Jun dimer is more stable than other dimeric proteins that have been studied, with a K_d of 54 nM, and thus might be expected to prefer the dimer DNA binding pathway. Second, Fos and Jun bind DNA as a heterodimer, rather than as a homodimer. Consequently, DNA binding has the potential to occur through one of three pathways, the monomer pathway with Jun binding DNA first (Jun pathway), the monomer pathway with Fos binding DNA first (Fos pathway), or the pathway in which dimerization precedes DNA binding (dimer pathway).

We used stopped-flow fluorescence resonance energy transfer (FRET) to study the dimerization kinetics of Fos and Jun, in the absence and presence of DNA. Though the two proteins formed a heterodimer rapidly, the rate of dimerization was accelerated in the presence of DNA. Simulations show that the dimer pathway is unable to account for the observed kinetics. We propose that Fos and Jun bind DNA through one or both monomer pathways, perhaps preferring the pathway in which Jun binds DNA first.

EXPERIMENTAL PROCEDURES

Materials. Bromoacetamide was purchased from Sigma. 5-Iodoacetamidofluorescein (5-IAF) and single isomer 5-iodoacetamidotetramethylrhodamine (5-TMRA) were purchased from Molecular Probes. KH_2PO_4, Na_2HPO_4, KCl, and NaCl used to make buffers for fluorescence experiments were purchased from Panvera Corporation (WI). Calf thymus DNA was purchased from Gibco. BSA was purchased from New England BioLabs.

PBS is phosphate-buffered saline; a 1× solution consists of 1.4 mM KH_2PO_4, 4.3 mM Na_2HPO_4, 2.7 mM KCl, and 137 mM NaCl, pH 7.4. The abbreviation 0.5× TBE refers to 45 mM Tris-Borate, 1 mM EDTA, pH 8.3 at 25 °C.

DNA. The DNA duplex AP-1_{23} contained the following sequence: 5′-AGTGGAGATGACTCATCTCGTGC-3′ and its complementary strand. The DNA duplex $cARRE_{29}$ contained the following sequence 5′-CCCCAAAGAG-GAAAATTTGACTCATACAG-3′ and its complementary strand. Oligonucleotides were synthesized on a 0.2 μmol scale at the HHMI Biopolymer/Keck Foundation Biotechnology Resource Laboratory (Yale University School of Medicine, New Haven, CT). Crude oligonucleotides were purified by denaturing gel electrophoresis. For electrophoretic mobility shift assays, one strand of the DNA duplex was labeled at the 5′ end with γ-^{32}P-ATP. Complementary strands were annealed together to form duplex DNA.

Peptide Sequences. The peptide JunC contained residues 263−324 of human cJun (*28*). Similarly, FosC contained residues 139−200 of human cFos (*29*). Both peptides contained two exogenous amino acids: an N-terminal methionine for bacterial expression and a C-terminal cysteine for sulfhydryl modification. Both peptides also contained a single mutation of the DNA-contact cysteine (C278 for cJun and C154 for cFos) to serine. This mutation has been shown to have no effect on the DNA binding properties of these proteins (*30*). The control peptide JunLZ contained residues 285−324 of human cJun followed by a C-terminal cysteine.

Production and Purification of Peptides. JunC and FosC were expressed in BL21 (DE3) pLysS *E. coli* (Novagen) from pET-3a expression plasmids (Stratagene). For each peptide, a culture of cells derived from a single colony was grown at 37 °C in M9ZB media containing 200 μg/mL ampicillin while shaking at 250 rpm. Protein expression was induced at an OD_{600} of 0.8 AU by addition of IPTG to a final concentration of 1 mM. Cells were harvested by centrifugation 3 h later. They were resuspended in 12.5 mL of lysis buffer (20 mM sodium HEPES, pH 7.9, 10% glycerol, 100 mM KCl, 5 mM $MgCl_2$, 1 mM PMSF, 0.1% NP-40, 100 mM DTT, 3 units/mL DNase I)/L of culture and lysed by boiling for 10 min. The lysate was clarified by centrifugation. Nucleic acids were precipitated with 0.5% PEI and removed by centrifugation. Peptides of interest were precipitated with $(NH_4)_2SO_4$ (80% saturation at 4 °C) and isolated by centrifugation. The precipitate was resuspended in 10 mM Tris, pH 7.5, 1 mM DTT and further purified by reversed-phase HPLC using a Vydac C_{18} column (10 × 250 mm). The identities of the peptides were verified by MALDI-TOF mass spectrometry (Voyager, Perseptive Biosystems). The observed molecular weights were as expected: JunC theoretical [MH+] = 7537.0, observed [MH+] = 7533.6; and FosC theoretical [MH+] = 7597.7, observed [MH+] = 7597.3. JunLZ was synthesized by the HHMI Biopolymer/Keck Foundation Biotechnology Resource Laboratory and purified by reversed-phase HPLC using a Vydac C_{18} column (10 × 250 mm). The theoretical mass, [MH+] = 4710.5, agreed with that observed by MALDI-TOF, [MH+] = 4710.9.

Sulfhydryl Modification of Peptides. Proteins were modified at unique cysteines to produce fluorescently labeled or alkylated products. The notation used is as follows: $FosC^{SR}$ indicates FosC alkylated with acetamide, $FosC^{SFlu}$ indicates

FosC alkylated with acetamidofluorescein, and FosC^{SRho} indicates FosC alkylated with acetamidotetramethylrhodamine. Analogous names are used for modified JunC and JunLZ.

Alkylation reactions used to produce FosC^{SR} or JunC^{SR} were performed by incubating 200 μM FosC or JunC in 20 mM sodium phosphate, pH 7.5 containing 8 mM bromoacetamide for 2 h at room temperature. FosC^{SR} and JunC^{SR} were purified by reversed-phase HPLC using a Vydac C_{18} column (10 × 250 mm). The observed masses, FosC^{SR} [MH+] = 7657 and JunC^{SR} [MH+] = 7597, agree with the theoretical masses, FosC^{SR} [MH+] = 7655 and JunC^{SR} [MH+] = 7589. The concentrations of FosC^{SR} and JunC^{SR} were determined by amino acid analysis at the HHMI Biopolymer/Keck Foundation Biotechnology Resource Laboratory.

FosC^{SFlu}, JunC^{SFlu}, and JunLZ^{SFlu} were produced by incubating 50 μM peptide in 50 mM sodium phosphate buffer, pH 7.5, containing 6.24 M guanidine HCl, 4 mM 5-iodoacetamidofluorescein and 2% dimethylformamide (DMF). The reaction was incubated in the dark at room temperature for 2−12 h. Unreacted fluorescein label was removed from the mixture by use of a NAP-10 column (Pharmacia) from which the peptide was eluted in 10 mM potassium phosphate, pH 7.1. Fluorescently labeled peptides were purified further by reversed-phase HPLC using a Vydac C_{18} column (10 × 250 mm). The observed masses FosC^{SFlu} [MH+] = 7989, JunC^{SFlu} [MH+] = 7929, and JunLZ^{SFlu} [MH+] = 5100, are in agreement with those predicted: FosC^{SFlu} [MH+] = 7985, JunC^{SFlu} [MH+] = 7918, and JunLZ^{SFlu} [MH+] = 5097. The concentrations of FosC^{SFlu}, JunC^{SFLu}, and JunLZ^{SFLu} were determined by amino acid analysis at the HHMI Biopolymer/Keck Foundation Biotechnology Resource Laboratory.

FosC^{SRho} was produced by incubating about 25 μM peptide in 50 mM sodium phosphate buffer, pH 7.5, containing 50 μM 5-iodoacetamidotetramethylrhodamine and 4% dimethylformamide. The reaction proceeded in the dark at room temperature for 12 h. The reaction mixture was subjected to multiple rounds of purification by reversed-phase HPLC (Vydac C_{18} column, 10 × 250 mm) in order to obtain a product of greater than 95% purity, the mass of which was determined to be 8044.0. The expected mass was 8040.0. The concentration of FosC^{SRho} was determined by amino acid analysis at the HHMI Biopolymer/Keck Foundation Biotechnology Resource Laboratory.

Measurement of the Critical Transfer Distance. The Forster radius, R_0, the distance at which fluorescence resonance energy transfer is 50% efficient, was calculated from the spectral properties of the donor and the acceptor according to eq 1 (*31*):

$$R_o = 9786(\kappa^2 n^{-4} Q_D J)^{1/6} \text{ (units in angstroms)} \quad (1)$$

In this equation, κ^2 represents the orientation of the donor and acceptor and is assumed to be $^2/_3$ for a randomly oriented donor−acceptor pair (*31*), and n represents the refractive index of the medium and has a value of 1.4 for proteins in water (*32*).

Q_D represents the quantum yield of the donor, which can be calculated according to eq 2 (*33*).

$$Q_D = Q_{RF}\left(\frac{I_D}{I_{RF}}\right)\left(\frac{A_{RF}}{A_D}\right) \quad (2)$$

In eq 2, I_D and I_{RF} represent the fluorescence intensities of the JunC^{SFlu} donor and the fluorescein reference, respectively; A represents the absorbance intensity of the reference compound, fluorescein, or of JunC^{SFlu}; and Q_{RF} represents the quantum yield of the reference [0.90 for fluorescein (*34*)].

J in eq 1 represents the degree of overlap between donor emission and acceptor absorbance spectra as calculated according to eq 3 (*31*).

$$J = \frac{\sum F(\lambda)\epsilon(\lambda)\lambda^4 \Delta\lambda}{\sum F(\lambda)\Delta\lambda} \quad (3)$$

In this equation, $F(\lambda)$ represents the measured fluorescence intensity of the JunC^{SFlu} donor and $\epsilon(\lambda)$ is the measured extinction coefficient of the FosC^{SRho} acceptor at wavelength λ. The absorbance spectrum of FosC^{SRho} and the emission spectrum of JunC^{SFlu} were measured between 500 and 600 nm ($\Delta\lambda$ = 1 nm). Values of $F(\lambda)$ and $\epsilon(\lambda)$ were tabulated and J was calculated.

Measurement of Fluorescence Resonance Energy Transfer Efficiency. The emission intensity at the wavelength of maximal donor emission was measured for the donor alone (I_D, 20 nM JunC^{SFlu}) and for the donor in the presence of a saturating amount of acceptor (I_{DA}, 20 nM JunC^{SFlu} and 500 nM FosC^{SRho}). The energy transfer efficiency (E) was calculated from the emission intesities according to eq 4 (*31*).

$$E = 1 - \frac{I_{DA}}{I_D} \quad (4)$$

The apparent distance separating the donor and the acceptor (R_{app}) was calculated according to eq 5 (*35*) using the values determined for R_0 and E:

$$R_{app} = R_0(E^{-1} - 1)^{1/6} \quad (5)$$

Equilibrium Fluorescence Measurements. Fluorescence emission scans were performed using a PTI QuantaMaster C-60 Spectrofluorimeter. Samples were incubated in 1× PBS buffer for 20 min at 25 °C then transferred to a 1 cm path length Hellma cuvette to acquire fluorescence spectra. The excitation wavelength was set to 490 nm using a 4 nm slit width, and emission was observed at 1 nm intervals from 500 to 600 nm using a 4 nm slit width and a 1 s sampling time. The spectra shown represent the averages of three scans of individual samples. The absorbance of buffer and/or nucleic acid components at 490 nm was always less than 0.005 absorbance units. The extent of fluorescence resonance energy transfer (FRET) was quantified by measuring the decrease in fluorescein emission at 515 nm. Fluorescence resonance energy transfer to rhodamine was verified by a fluorescence increase at 580 nm. However, as observed by others (*36*, *37*), the rhodamine emission (signal at 580 nm) was small relative to the fluorescein emission and resulted both from resonance transfer of energy from the fluorescein donor and from direct absorption of the 490 nm incident light. In both equilibrium and kinetic fluorescence measurements, the decrease in emission at 515 nm, rather than the

increase at 580 nm, was used quantify $FosC^{SRho}$·$JunC^{SFlu}$ complex formation.

The equilibrium dissociation constant for the $FosC^{SRho}$·$JunC^{SFlu}$ interaction was determined by monitoring the decrease in fluorescein emission at 515 nm as a function of $FosC^{SRho}$ concentration. The concentration of $JunC^{SFlu}$ was fixed at 20 nM, and the concentration of $FosC^{SRho}$ was varied from 28.2 to 1000 nM. The data were fit to eq 6 (*38*):

$$F_{obs} = F_{max} - \{(F_{max} - F_{min})/(2 \times [JunC^{SFlu}]_{tot})\}\{b - \sqrt{b^2 - 4[FosC^{SRho}]_{tot}[JunC^{SFlu}]_{tot}}\} \quad (6)$$

$$b = K_d + [JunC^{SFlu}]_{tot} + [FosC^{SRho}]_{tot}$$

where F_{obs} is the observed fluorescence for any mixture of $FosC^{SRho}$ and $JunC^{SFlu}$ and F_{max} and F_{min} are the maximum and minimum fluorescence intensities.

Fluorescence Anisotropy Measurements. Fluorescence anisotropy measurements were performed using a PTI QuantaMaster C-60 Spectrofluorimeter in the L-configuration. $JunC^{SR}$ or $FosC^{SR}$ was serially diluted in 1× PBS containing 50 nM $JunC^{SFlu}$. The fluorescence anisotropy of each sample was measured by excitation with vertically polarized light at wavelength of 490 nm (10 nm slit width) and the fluorescence emission was measured at 520 nm (10 nm slit width) in the horizontal and vertical directions for 60 s time periods. Anisotropy was calculated from the fluorescence intensities in the parallel ($I_{||}$) and perpendicular ($I_{\perp}$) directions according to the relationship $A = (I_{||} - I_{\perp})/(I_{||} + 2I_{\perp})$ (*39*). The anisotropy values for between two and four independent sets of samples were averaged.

The anisotropy was plotted versus the concentration and the data was fit to eq 7 (*40*) to determine the K_d for Jun homodimer formation or to eq 8 to determine the K_d for Fos·Jun heterodimer formation.

$$A_{obs} = A_{min} + \left\{(A_{max} - A_{min})\left[\frac{\sqrt{K_d^2 + (8K_d[JunC^{SFlu} + JunC^{SR}])} - K_d}{4[JunC^{SFlu} + JunC^{SR}]}\right]\right\} \quad (7)$$

$$A_{obs} = A_{min} + \{(A_{max} - A_{min})/(2 \times [JunC^{SFlu}])\}\{b - \sqrt{b^2 - 4[FosC^{SRho}][JunC^{SFlu}]}\} \quad (8)$$

$$b = K_d + [JunC^{SFlu}] + [FosC^{SRho}]$$

In eqs 7 and 8, A_{obs} is the observed anisotropy for any peptide concentration, A_{max} is the maximum observed anisotropy, and A_{min} is the minimum observed anisotropy. K_d is the equilibrium dissociation constant.

Stopped-Flow Fluorescence Measurements. Stopped-flow fluorescence experiments were performed on a KinTek SF-2001 stopped-flow spectrophotometer. Fluorescein was excited at 495 nm using a 2 nm slit width and a Xenon short arc lamp light source (Ushio, Japan). The time-dependent change in fluorescein emission was monitored at 520 nm, using a 10 nm band-pass filter (Corion, Franklin, MA). Fluorescein- and rhodamine-labeled peptides were incubated in 1× PBS and loaded into two 5 mL syringes through their individual loading ports. A third, 0.5 mL, syringe was loaded with 1× PBS or nucleic acid. Three-way mixing was initiated by injecting samples through a microjet mixer at a flow rate of 6 mL/s before the reaction mixture reached the 20 μL observation cell. A high-torque stepper motor drive with dead time of less than 1 ms was used to control the injection. Data shown are the average of three to six individual traces.

To determine the rate constants describing the interaction of $JunC^{SFlu}$ with $FosC^{SRho}$, the two peptides were rapidly mixed such that the final concentration of $JunC^{SFlu}$ was 20 nM and the final concentration of $FosC^{SRho}$ was 20, 50, 250, or 500 nM. The changes in fluorescence emission intensity as a function of time for the four different ratios of $JunC^{SFlu}$:$FosC^{SRho}$ were fit globally to the molecular mechanism shown in eq 9 using nonlinear least-squares regression provided by the Dynafit computer algorithm (*41*).

Simulation of Binding Kinetics. Model discrimination analysis using the Dynafit algorithm was used to distinguish among potential mechanisms of DNA binding. Six equations were used to describe all potential equilibria:

$$JunC^{SFlu} + FosC^{SRho} \underset{k_{d1r}}{\overset{k_{d1f}}{\rightleftharpoons}} JunC^{SFlu}\cdot FosC^{SRho} \quad (9)$$

$$JunC^{SFlu}\cdot FosC^{SRho} + DNA \underset{k_{d2r}}{\overset{k_{d2f}}{\rightleftharpoons}} JunC^{SFlu}\cdot FosC^{SRho}\cdot DNA \quad (10)$$

$$FosC^{SRho} + DNA \underset{k_{f1r}}{\overset{k_{f1f}}{\rightleftharpoons}} FosC^{SRho}\cdot DNA \quad (11)$$

$$JunC^{SFlu} + FosC^{SRho}\cdot DNA \underset{k_{f2r}}{\overset{k_{f2f}}{\rightleftharpoons}} JunC^{SFlu}\cdot FosC^{SRho}\cdot DNA \quad (12)$$

$$JunC^{SFlu} + DNA \underset{k_{j1r}}{\overset{k_{j1f}}{\rightleftharpoons}} JunC^{SFlu}\cdot DNA \quad (13)$$

$$FosC^{SRho} + JunC^{SFlu}\cdot DNA \underset{k_{j2r}}{\overset{k_{j2f}}{\rightleftharpoons}} JunC^{SFlu}\cdot FosC^{SRho}\cdot DNA \quad (14)$$

Seven models were considered, each of which included one or more of the three potential DNA binding pathways. The *dimer pathway* represents dimerization of Fos and Jun followed by DNA binding. The *Fos pathway* represents DNA binding by Fos followed by recruitment of Jun to form the final complex. The *Jun pathway* represents DNA binding by Jun followed by recruitment of Fos to form the final complex. The equations used for the seven models were as follows: dimer, eqs 9 and 10; Fos, eqs 9, 11, and 12; Jun, eqs 9, 13, and 14; dimer + Fos, eqs 9−12; dimer + Jun, eqs 9, 10, 13, and 14; Fos + Jun, eqs 9 and 11−14; dimer + Fos + Jun, eqs 9−14.

Sixteen kinetic traces containing varying concentrations of $FosC^{SRho}$, $JunC^{SFlu}$, and calf thymus DNA were fit simultaneously to each model and the appropriate parameters were optimized. (The Dynafit algorithm is limited to the simultaneous simulation of 16 data sets. Twenty different data sets were considered. The results exhibited little variation depending on which data sets were included, indicative of the robustness of the simulation.) Optimizable parameters included the relevant rate constants and the maximum and minimum fluorescence response. The ratio

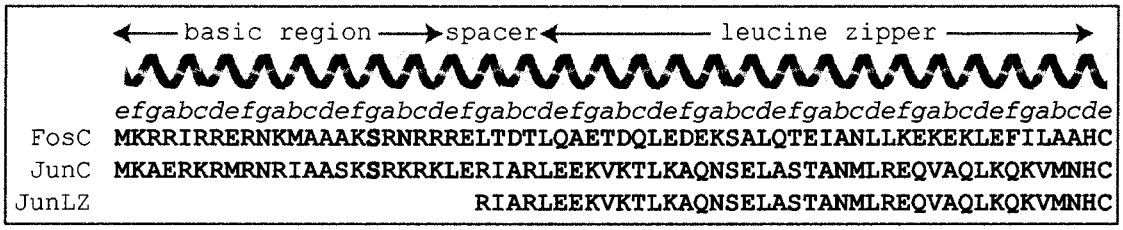

FIGURE 2: Amino acid sequences of peptides used in this study. FosC contains the basic region, spacer and leucine zipper of cFos with a C-terminal cysteine. JunC contains the basic region, spacer and leucine zipper of cJun with a C-terminal cysteine. JunLZ contains the spacer and leucine zipper of cJun with a C-terminal cysteine. Shown above the sequences is the heptad repeat (*abcdefg*) indicative of the residues' axial positions on the helix.

of k_{d1r}/k_{d1f} was fixed at 5.4×10^{-8} M, the equilibrium dissociation constant of the $FosC^{SRho}$·$JunC^{SFlu}$ complex as determined by equilibrium fluorescence titration. The ratios $k_{d1r}k_{d2r}/k_{d1f}k_{d2f}$, $k_{f1r}k_{f2r}/k_{f1f}k_{f2f}$, and $k_{j1r}k_{j2r}/k_{j1f}k_{j2f}$ were set to 1.2×10^{-16} M^2, the overall affinity of the Fos·Jun dimer for DNA as determined by electrophoretic mobility shift assay (*42*). On the basis of equilibrium fluorescence spectra, the molar fluorescence response of the $FosC^{SRho}$·$JunC^{SFlu}$ complex was set to be equal to that of the $FosC^{SRho}$·$JunC^{SFlu}$·DNA complex. Similarly, the molar fluorescence responses of $JunC^{SFlu}$ and of $JunC^{SFlu}$·DNA were set to be equal.

For each model the best values of the optimizable parameters were determined by nonlinear least-squares regression using the Levenberg−Marquardt algorithm included in Dynafit (*41*). The Dynafit program then used seven statistical criteria to assess the goodness of fit of each model and its optimized parameters and selected the best model based on the statistical criteria. One statistical criterium used to compare the quality of fits achieved with different models is the summed least squares residuals. The significance of differences between values of summed least squares residuals was evaluated by comparing the calculated *F* ratios to the critical values of *F* at the 95% probability level. This analysis accounts for unequal numbers of parameters in different models.

Electrophoretic Mobility Shift Assays. Serial dilutions of $FosC^{SR}$ + $JunC^{SR}$ or $FosC^{SRho}$ + $JunC^{SFlu}$ were incubated with <50 pM γ-[^{32}P]-DNA in 1× binding buffer [1× PBS containing 0.1% (v/v) Nonidet P-40, 5% (v/v) glycerol, 400 μg/mL BSA, 1 mM EDTA] for 30 min at 25 °C. Individual samples were loaded onto a nondenaturing 8% [49:1 acrylamide:bis(acrylamide)] gel prepared in 0.5× TBE. Gels were run at 500 V for 40 min at 25 °C. Dried gels were exposed overnight to phosphor storage screens which were then scanned using a STORM 840 Phosphorimager (Molecular Dynamics). Radioactivity was quantified using ImageQuant 5.0 software (Molecular Dynamics). The fraction of DNA bound was plotted versus total peptide concentration and the data fit to the Langmuir equation [fraction DNA bound = $1/(1 + K_{app}/[\text{peptide}]_{total}^2)$] to determine the equilibrium dissociation constant (*42*).

Kinetic analysis was performed by incubating peptides in 145 μL of 1× binding buffer for 30 min at 25 °C. Binding was initiated by addition of 5 μL of 1.5 nM ^{32}P end-labeled DNA in 1× binding buffer. Aliquots (8 μL) of the reaction mixture were loaded onto a running gel at 10 s intervals. Gels were run and analyzed as for equilibrium experiments. The dead time for this experiment is no more than 30 s (*15*).

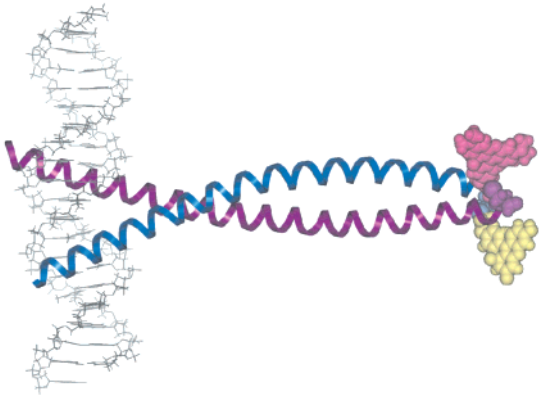

FIGURE 3: $FosC^{SRho}$·$JunC^{SFlu}$·AP-1 complex. Coordinates for Fos, Jun, and DNA were derived from the crystal structure of the complex, with additional amino acids modeled in alpha-helical conformation. The C-terminal cysteines were further modified with acetamidofluorescein and acetamidotetramethylrhodamine. Fluorophores are shown oriented away from the leucine zipper; however, the structure is not minimized; this depiction represents one of many possible conformations that the complex may assume. Fos is shown as a purple ribbon with its appended cysteine in purple CPK representation. The rhodamine label is shown in pink CPK representation. Jun is shown as a blue ribbon with its appended cysteine in blue CPK representation. The fluorescein label is shown in yellow CPK representation. DNA is shown in gray.

RESULTS

Experimental Design. Dimerization kinetics of Fos and Jun in the absence and presence of DNA were determined by monitoring the rate of fluorescence resonance energy transfer (FRET) (*31*) between a Jun construct labeled with fluorescein and a Fos construct labeled with rhodamine. Protein constructs (JunC and FosC) contained a C-terminal cysteine for fluorophore labeling and comprised the 63 amino acid bZIP elements of cJun and cFos (Figure 2), respectively. Each construct also contained serine in place of the basic region cysteine found in the native sequence (*30*). JunC was modified with the fluorophore acetamidofluorescein to yield the conjugate $JunC^{SFlu}$, and FosC was modified with acetamidotetramethylrhodamine to yield $FosC^{SRho}$.

The modified cysteines are located three amino acids beyond the most C-terminal residues visible in the crystal structure of Fos and Jun complexed with their target DNA site (*43*) (in the *e* positions of each leucine zipper, Figure 2). When the additional C-terminal residues are modeled onto the structure in α-helical conformation, the distance between the cysteine sulfur atoms of FosC and JunC is about 13 Å (Figure 3). Adding in the additional length through the linker to the center of each fluorescent probe, we arrived at an

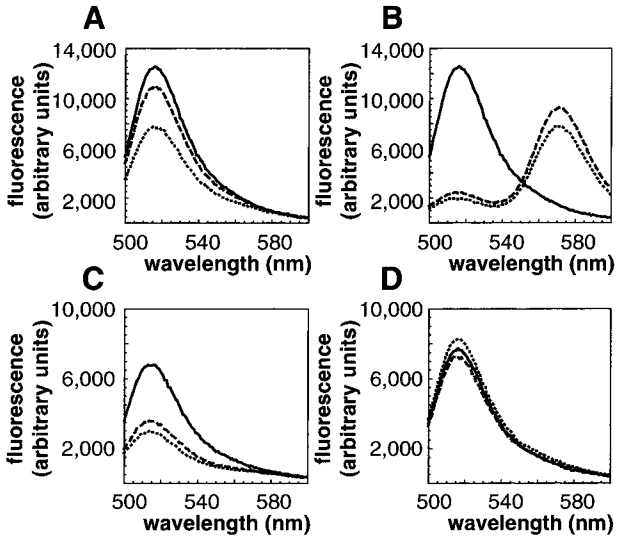

FIGURE 4: Quenching of JunC^{SFlu} fluorescence depends on its dimerization with FosC^{SRho} and can be induced by DNA binding. (A) Fluorescence spectra showing 20 nM JunC^{SFlu} alone (solid line) and in the presence of 20 nM FosC^{SRho} (dashed line) or 20 nM FosC^{SRho} and 100 nM cARRE$_{29}$ (dotted line). (B) Fluorescence spectra showing 20 nM JunC^{SFlu} alone (solid line) and in the presence of 500 nM FosC^{SRho} (dashed line) or 500 nM FosC^{SRho} and 100 nM cARRE$_{29}$ (dotted line). (C) Fluorescence spectra showing 20 nM JunLZ^{SFlu} alone (solid line) and in the presence of 20 nM FosC^{SRho} (dashed line) or 20 nM FosC^{SRho} and 100 nM cARRE$_{29}$ (dotted line). (D) Fluorescence spectra showing 20 nM FosC^{SFlu} alone (solid line) and in the presence of 20 nM FosC^{SRho} (dashed line) or 20 nM FosC^{SRho} and 100 nM cARRE$_{29}$ (dotted line).

expected R value of 33 Å for the separation distance between the fluorescent probes.

We determined the R_0 for our fluorescence donor−acceptor pair, JunC^{SFlu} and FosC^{SRho}, based on measured values of Q_D and J. JunC^{SFlu} had a quantum yield ($Q_D = 0.45$) similar to other fluorescein-modified proteins (*35*, *44*). Likewise, the spectral overlap between the fluorescence emission spectrum of JunC^{SFlu} and the absorption spectrum of FosC^{SRho} ($J = 1.91 \times 10^{-13}$ M^{-1} cm^3) was similar to values published elsewhere for the fluorescein-tetramethylrhodamine pair (*44*). The resulting value of R_0, 48.5 Å, was in agreement with previously published values (*35*, *44*) and indicates that these molecules should be suitable for probing the association of Fos and Jun.

Fluorescein Quenching Is a Measure of Fos·Jun Dimer Formation. The ability of the fluorescein-rhodamine FRET system to serve as a useful probe of Fos·Jun dimer formation was determined by equilibrium fluorescence experiments. The fluorescein emission of JunC^{SFlu} is quenched in the presence of FosC^{SRho} (Figures 4, panels A and B, and 5A), indicative of dimer formation. At concentrations where JunC^{SFlu} and FosC^{SRho} are incompletely dimerized, the addition of DNA containing the AP1 target site (cARRE$_{29}$) increases dimer formation and thereby increases the observed amount of fluorescence resonance energy transfer. For example, the fluorescein emission of 20 nM JunC^{SFlu} is quenched by 20 nM FosC^{SRho} and quenched further in the presence of 100 nM cARRE DNA (Figure 4A). In contrast, under conditions where nearly all of the JunC^{SFlu} forms heterodimers with FosC^{SRho} (20 nM JunC^{SFlu} and 500 nM FosC^{SRho}), 100 nM cARRE$_{29}$ DNA has little effect on the fluorescein emission (515 nm) of JunC^{SFlu} (Figure 4B). Quenching induced by the presence of DNA is dependent upon DNA binding. Fluorescein emission of the construct JunLZ^{SFlu}, which does not contain a basic region (Figure 2), is quenched by the addition of FosC^{SRho}, but addition of cARRE$_{29}$ DNA does not cause significant further quenching (Figure 4C).

The induced quenching of JunC^{SFlu} by FosC^{SRho} in the presence of DNA is not restricted to use of cARRE$_{29}$ DNA. Similar quenching of JunC^{SFlu} by FosC^{SRho} can be induced by the presence of calf thymus DNA (data not shown). Calf thymus DNA contains a distribution of DNA sequences some of which are likely to be similar or identical to the AP-1 site, and some of which will be completely nonspecific. We used calf thymus DNA in all stopped-flow fluorescence experiments for two reasons. Not only was it was easily obtainable in the desired quantities but also earlier studies of Arc repressor kinetics had shown that long nucleic acid polymers were more effective than short oligonucleotides at enhancing the observed dimerization rate of Arc (*20*).

Control experiments were performed to verify that the observed quenching of JunC^{SFlu} fluorescence depends on the presence of Fos and on the tetramethylrhodamine label that serves as a FRET acceptor. The bHLHZip protein Max, which is not expected to form a heterodimer with Jun (*11*), does not quench JunC^{SFlu} fluorescence (data not shown). Additionally, FosC^{SRho} only quenches fluorescein-labeled proteins with which it dimerizes well. FosC^{SRho} does not quench fluorescein-labeled Fos (FosC^{SFlu}), even in the presence of cARRE$_{29}$ DNA (Figure 4D), consistent with previous work showing that Fos·Fos homodimers are unstable [$K_d \approx 6$ μM (*45*−*47*)].

The efficiency of energy transfer was calculated from the spectra of fluorescent donor alone (20 nM JunC^{SFlu}) and with a saturating concentration of acceptor (20 nM JunC^{SFlu} and 500 nM FosC^{SRho}). The analysis produced an efficiency value, E, of 81%. The efficiency of transfer, when combined with the R_0 measured for this pair, allowed us to estimate the distance, R_{app}, between the fluorophores in the JunC^{SFlu}·FosC^{SRho} complex to be about 38 Å. The apparent distance agreed well with the value predicted from the crystal structure ($R = 33$ Å).

Equilibrium Fluorescence Analysis of Dimer Stability. The ability of FosC^{SRho} and JunC^{SFlu} to form heterodimers was assayed quantitatively by FRET. Figure 5A shows that JunC^{SFlu} fluorescence at 515 nm is quenched in saturable manner upon dimerization with FosC^{SRho}. By fitting the data shown in Figure 5A to eq 8, the equilibrium dissociation constant (K_d) of the FosC^{SRho}·JunC^{SFlu} heterodimer was calculated to be 54 ± 12 nM. This value agrees well with previously reported values measured either by FRET between fluorescently labeled basic region cysteines [$K_d = 23 \pm 9$ nM (*48*)] or by scintillation proximity assay [$IC_{50} = 110 \pm 12$ nM (*49*)].

We also used fluorescence polarization to verify the K_d for Fos·Jun heterodimer formation (Figure 5B). Fluorescently labeled Jun (JunC^{SFlu}) was incubated with varying concentrations of nonfluorescent Fos (FosC^{SR}) and the change in the anisotropy of JunC^{SFlu} fluorescence was monitored. These data were fit to eq 8 to determine an equilibrium dissociation constant of 106 ± 40 nM. The K_d values determined by the two different methods differ by less than a factor of 2 and

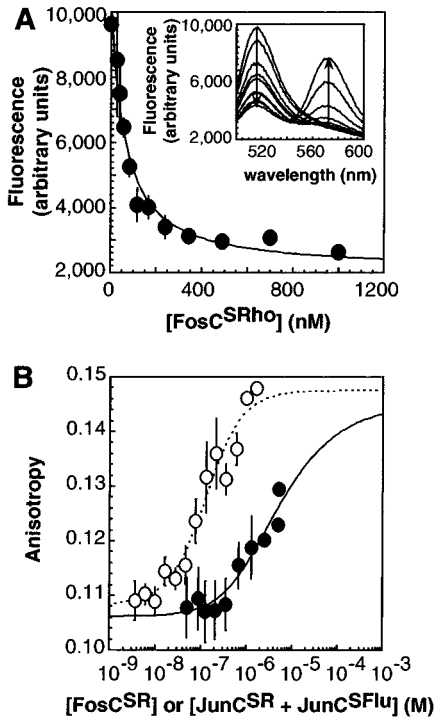

FIGURE 5: (A) Use of fluorescence resonance energy transfer to determine the K_d for $JunC^{SFlu}$·$FosC^{SRho}$ binding. Fluorescence at 515 nm was plotted as a function of $FosC^{SRho}$ concentration. Each point is the average value obtained from fluorescence spectra acquired using three separate samples; error bars denote the standard error. The solid line shows the fit to eq 8, from which the K_d (54 ± 12 nM) was determined. (Inset) Spectra showing decrease in $JunC^{SFlu}$ fluorescence as a function of $FosC^{SRho}$ concentration. All samples contain 1× PBS and 20 nM $JunC^{SFlu}$. The concentration of $FosC^{SRho}$ varies up to 1 μM. (B) The K_ds for Fos·Jun heterodimer formation and Jun·Jun homodimer formation were determined by fluorescence polarization. Serial dilutions of $FosC^{SR}$ or $JunC^{SR}$ were mixed with 50 nM JunCSFlu in 1× PBS. The fluorescein polarization was measured and plotted versus [$FosC^{SR}$] (open circles) or [$JunC^{SR}$ + $JunC^{SFlu}$] (filled circles). Data were fit to eq 8 (dashed line) or 7 (solid line) to determine the K_d for Fos·Jun heterodimer formation (106 ± 40 nM) or to estimate the K_d for Jun·Jun homodimer formation (4.7 ± 4.1 μM).

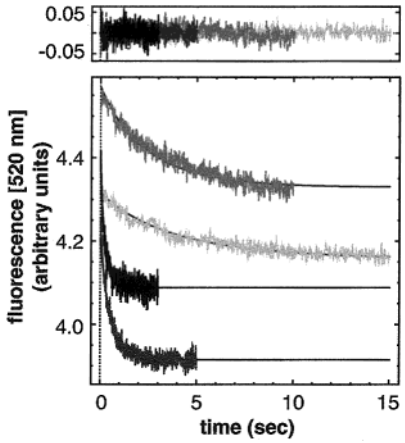

FIGURE 6: Stopped-flow kinetic measurement of $JunC^{SFlu}$ binding to $FosC^{SRho}$. The time-dependent fluorescence change observed at 520 nm when $JunC^{SFlu}$ (20 nM final concentration) is mixed with $FosC^{SRho}$ (final concentration 500 nM, black trace; 250 nM, dark gray trace; 50 nM, medium gray trace; 20 nM, light gray trace). The fits shown are the global best fit calculated by the program Dynafit (*41*) using a two-state binding model. The single set of rate constants best describing all four kinetic traces is $k_{1df} = 7.36 \pm 0.11 \times 10^6\ M^{-1}\ s^{-1}$ and $k_{1dr} = 0.064 \pm 0.003\ s^{-1}$. The residuals shown above the plot are the difference between the observed data and the global best fit curves; they are small and randomly distributed about zero.

Table 1: Relaxation Rates and Amplitudes Characterizing $JunC^{SFlu}$ Quenching Occurring upon Formation of $JunC^{SFlu}$·$FosC^{SRho}$ Dimers[a]

[$FosC^{SRho}$] (nM)	τ (s^{-1})	A (arbitrary units)
20	0.26 ± 0.01	0.144 ± 0.002
50	0.28 ± 0.01	0.228 ± 0.003
250	2.09 ± 0.04	0.319 ± 0.004
500	4.2 ± 0.1	0.300 ± 0.006

[a] $JunC^{SFlu}$ concentration in all cases was 20 nM.

are within the error of each other. We chose to use the value of 54 nM for subsequent kinetics experiments because (1) it measures the same physical parameter, FRET, as the stopped-flow experiments, and (2) it predicts the larger population of dimers, which will be the limiting variable in later simulations.

To minimize off-pathway events that might complicate analysis of our time-resolved experiments, we sought to keep the $JunC^{SFlu}$ concentration low enough to avoid significant formation of $JunC^{SFlu}$·$JunC^{SFlu}$ homodimers. Toward this end, we measured the fluorescence polarization of a mixture of $JunC^{SR}$ and $JunC^{SFlu}$ to estimate the amount of Jun·Jun homodimers formed. On the basis of the concentration dependence of fluorescence polarization, the K_d of the $JunC^{SFlu}$ homodimer was estimated to be no less than 600 nM (Figure 5B). (Fluorescence polarization measurements made using only fluorecein-labeled Jun estimate the K_d for Jun·Jun dimer formation to be 2.0 μM, data not shown.) Our measurements agree with the value measured previously by a scintillation proximity assay, which showed the IC_{50} for the Jun·Jun interaction to be 476 ± 15 nM (*49*). The polarization data also shows that no significant population of Jun·Jun dimers form at a total peptide concentration of 100 nM. The concentration of $JunC^{SFlu}$ was allowed to vary no higher than 100 nM in subsequent fluorescence experiments. Therefore, though our Jun·Jun K_d determination was not of high accuracy, it sufficed to verify that Jun·Jun dimer formation was not significant within the concentration range of our experiments. Fos homodimers are less stable [$K_d \approx 6$ μM (*45*)] than Jun homodimers, so the concentration of $FosC^{SRho}$ could vary as high as 500 nM in equilibrium fluorescence and stopped-flow fluorescence experiments without concern that a significant population of $FosC^{SRho}$·$FosC^{SRho}$ dimers was being formed.

Kinetics of Fos·Jun Dimerization. The rate of dimerization between $FosC^{SRho}$ and $JunC^{SFlu}$ was measured by stopped-flow fluorescence. Rapid mixing of $FosC^{SRho}$ and $JunC^{SFlu}$ resulted in a time-dependent decrease in fluorescein emission (Figure 6). Both the rate of decrease in fluorescein emission and the amplitude of the decrease depended upon the concentration of $FosC^{SRho}$. For all concentrations of $FosC^{SRho}$, the kinetic traces could be fit well by a single-exponential curve. The relaxation rates and amplitudes obtained from fits of each trace to a single exponential are shown in Table 1. The relaxation rate, τ, varies about 15-fold, from 0.26 to 4.2 s^{-1}, over a 25-fold range in $FosC^{SRho}$ concentration. The amplitude more than doubles over the same concentration range, from 0.144 to 0.319, due to increased heterodimer formation at higher $FosC^{SRho}$ concentrations. Our data are

characterized by half-times between 0.74 and 1.35 s. Thus, they are consistent with previous kinetics studies using Fos and Jun peptides labeled with a fluorescence donor and acceptor, respectively. These experiments showed that dimerization occurs rapidly, with a half-time of <10 s (*48*).

To determine the rate constants defining the first step in the dimer binding pathway (k_{d1f} and k_{d1r}, eq 9), the kinetic traces (Figure 6) describing the association of $JunC^{SFlu}$ with four different concentrations of $FosC^{SRho}$ were analyzed simultaneously using the program Dynafit (*41*). This program uses a least-squares minimization algorithm defined by a hypothetical model to find the single set of rate constants which best describes all four traces. In this case, a two-state model (eq 9) representing formation of the $FosC^{SRho}$·$JunC^{SFlu}$ heterodimer from monomeric $FosC^{SRho}$ and $JunC^{SFlu}$ was used. The best fit to all four kinetic traces resulted in rate constants of $k_{1df} = (7.36 \pm 0.11) \times 10^6\ M^{-1}\ s^{-1}$ and $k_{1dr} = 0.064 \pm 0.003\ s^{-1}$ and is indicated by the black solid lines in Figure 6. These rate constants produced a good fit to the data: the residuals are small and randomly distributed about zero (Figure 6). Moreover, the algorithm converged to the same rate constants when any one trace was excluded from the fit, indicating that the values were overdetermined.

Fos and Jun Bind DNA Rapidly. The affinity of the $FosC^{SR}$·$JunC^{SR}$ heterodimer for DNA containing the AP-1 target site ($AP1_{23}$) was measured by electrophoretic mobility shift assay. Analysis of the binding curve (*42*) defined a value of $1.6 \times 10^{-16}\ M^2$ for K_{app}, corresponding to half-maximal binding occurring at 12.0 nM (Figure 7A). The rate at which the Fos·Jun·DNA complex formed was assayed initially by time-resolved electrophoretic mobility shift experiments. At all peptide concentrations tested (150, 75, 37.5, 18.8, 9.38, and 4.69 nM) $AP1_{23}$ binding occurred too rapidly to be measured by this assay (Figure 7B), which has a lag time of <30 s (*15*).

DNA Enhances the Rate of Dimer Formation. The rate at which $FosC^{SRho}$ quenches the fluorescence of $JunC^{SFlu}$ was increased in the presence of calf thymus DNA (Figure 8A and Table 2). Whereas the time-dependent fluorescence decrease observed upon mixing $JunC^{SFlu}$ and $FosC^{SRho}$ was described well by a single exponential, the decrease in fluorescence observed in the presence of DNA was fit well only by a double exponential. The double exponential observed in the presence of DNA describes two rates, a slow rate which is similar to that observed in the absence of DNA and a fast rate that generally increases with increasing DNA concentration (Table 2). As judged by the relative values of A_1 and A_2, the contribution of the slow rate to the total fluorescence change generally decreases with increasing DNA concentration while the contribution of the fast rate increases.

By the following logic, we interpret the slow rate to represent dimerization of $FosC^{SRho}$ and $JunC^{SFlu}$ occurring off DNA and the fast rate to represent dimerization of $FosC^{SRho}$ and $JunC^{SFlu}$ occurring on DNA. First, at any set of $FosC^{SRho}$ and $JunC^{SFlu}$ concentrations, the slow component of the double exponential observed in the presence of DNA has the same relaxation rate as the single exponential observed in the absence of DNA. This relationship holds through a 100-fold range of DNA concentrations, suggesting that the slow component of the double exponential describes the process (dimerization) that occurs in the absence of DNA.

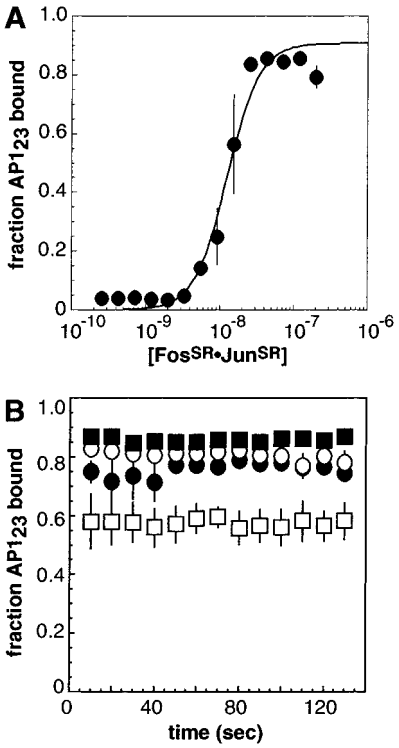

FIGURE 7: Assessment of DNA binding by Fos and Jun. (A) The affinity of the $FosC^{SR}$·$JunC^{SR}$ heterodimer for DNA was measured by quantitative electrophoretic mobility shift assay. The fraction of DNA bound is shown plotted versus the peptide concentration. The solid curve shows the best fit to the Langmuir equation [fraction DNA bound = $1/(1 + K_{app}/[peptide]_{total}^2)$]. K_{app} determined from this fit was $1.6 \pm 0.3 \times 10^{-16}\ M^2$. (B) Electrophoretic mobility shift assays show that $JunC^{SR}$·$FosC^{SR}$·AP-1_{23} complex formation occurs rapidly. Solutions of $JunC^{SR}$ and $FosC^{SR}$ were rapidly mixed with < 50 pM ^{32}P-AP-1_{23} at time zero and aliquots were loaded on the gel at 10 second intervals. The concentrations of peptides used were: filled circles, 150 nM $JunC^{SR}$ + 150 nM $FosC^{SR}$; open circles, 75 nM $JunC^{SR}$ + 75 nM $FosC^{SR}$; filled squares, 37.5 nM $JunC^{SR}$ + 37.5 nM $FosC^{SR}$; open squares, 18.75 nM $JunC^{SR}$ + 18.75 nM $FosC^{SR}$. The fraction of DNA bound by $JunC^{SR}$·$FosC^{SR}$ is plotted at each time point. Each point represents the average of four independent experiments; error bars denote the standard error.

If the slow rate represents dimerization of $FosC^{SRho}$ and $JunC^{SFlu}$ occurring off DNA, then the fast rate must represent dimerization of $FosC^{SRho}$ and $JunC^{SFlu}$ occurring on the DNA. (The fast rate cannot represent binding of preformed dimers to DNA for two reasons. One, binding of preformed dimers to DNA results in little or no additional fluorescence change (Figure 4B). Two, even if the rate of dimer binding to DNA were faster than the rate of dimerization, the rate of dimerization would remain the limiting step.) Dimerization on the DNA offers an explanation for the dependence of the fast phase (both its rate and magnitude) on DNA concentration. As DNA concentration increases, dimerization proceeds more rapidly and a larger fraction of the fluorescence change results from DNA-mediated dimerization. For example, when 50 nM $JunC^{SFlu}$ is mixed with 200 nM $FosC^{SRho}$ (Figure 8A) in the absence of calf thymus DNA, none of the fluorescence change results from DNA-mediated dimerization. When 50 nM calf thymus DNA is present, 46% of the fluorescence change results from DNA-mediated dimerization. The percentage of fluorescence change due to DNA-mediated dimerization increases further in the presence of 500 nM and 5 μM calf thymus DNA. (In some cases, the amplitude of

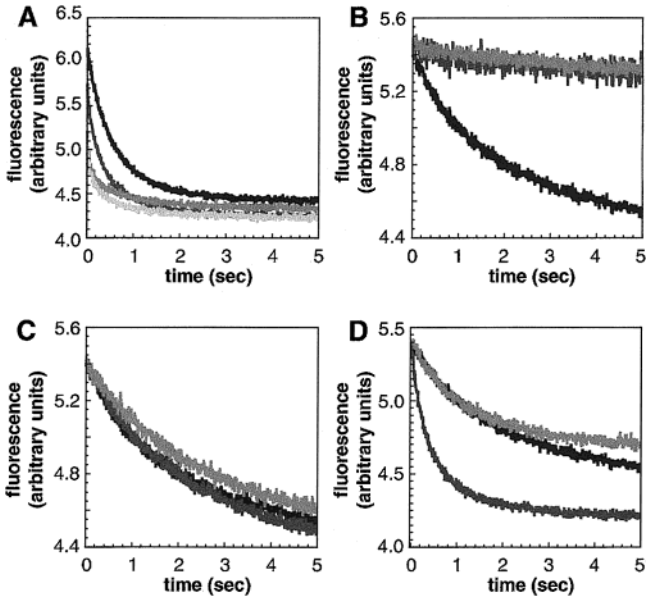

FIGURE 8: Stopped-flow fluorescence measurement of the rate of complex formation. Shown is the time-dependent fluorescence change observed at 520 nm. (A) Fluorescein quenching observed upon rapid mixing of 50 nM $JunC^{SFlu}$ and 200 nM $FosC^{SRho}$ (black trace), 50 nM $JunC^{SFlu}$, 200 nM $FosC^{SRho}$ and 50 nM bp calf thymus DNA (dark gray trace), 50 nM $JunC^{SFlu}$, 200 nM $FosC^{SRho}$ and 500 nM bp calf thymus DNA (medium gray trace), 50 nM $JunC^{SFlu}$, 200 nM $FosC^{SRho}$ and 5 μM bp calf thymus DNA (light gray trace). (B) Fluorescein quenching observed upon rapid mixing of 20 nM $JunC^{SFlu}$ and 100 nM $FosC^{SRho}$ (black trace), 20 nM $FosC^{SFlu}$ and 100 nM $FosC^{SRho}$ (dark gray trace), and 20 nM $FosC^{SFlu}$, 100 nM $FosC^{SRho}$, and 200 nM bp calf thymus DNA (medium gray trace). (C) Fluorescein-quenching observed upon rapid mixing of 20 nM $JunC^{SFlu}$ and 100 nM $FosC^{SRho}$ (black trace), 20 nM $JunLZ^{SFlu}$ and 100 nM $FosC^{SRho}$ (dark gray trace), and 20 nM $JunLZ^{SFlu}$, 100 nM $FosC^{SRho}$, and 2 μM bp calf thymus DNA (medium gray trace). (D) Fluorescein quenching observed upon rapid mixing of 20 nM $JunC^{SFlu}$ and 100 nM $FosC^{SRho}$ (black trace), 20 nM $JunC^{SFlu}$, 100 nM $FosC^{SRho}$, and 500 nM bp calf thymus DNA (dark gray trace), and 20 nM $JunC^{SFlu}$, 100 nM $FosC^{SRho}$ and 1 μM deoxyribonucleotides (medium gray trace).

the fast phase appears to decrease with increasing DNA concentration. This is observed when fluorescence quenching occurs so rapidly that the early time points are not observed. We did not attempt to correct for this artifact, but expect that it would cause us to *underestimate* the rate at which dimers form in the presence of calf thymus DNA.)

As demonstrated in equilibrium experiments, the quenching of $FosC^{SRho}$ fluorescence by $JunC^{SFlu}$ occurs only upon formation of the heterodimer. When fluorescein-labeled Fos ($FosC^{SFlu}$) is mixed with $FosC^{SRho}$, essentially no fluorescence change is observed (Figure 8B, Table 3) because Fos does not form homodimers. Furthermore, the presence of calf thymus DNA has no effect on the observed fluorescence of a mixture of $FosC^{SFlu}$ and $FosC^{SRho}$ because DNA does not template the formation of Fos homodimers.

The DNA-mediated increase in the rate of dimer formation is observed only when peptides contain basic regions capable of recognizing DNA. When a fluorescein-labeled peptide containing the leucine zipper but not the basic region of Jun ($JunLZ^{SFlu}$) is mixed with $FosC^{SRho}$, a time-dependent decrease in fluorescence is observed (Figure 8C). This decrease is fit by single exponential (0.47 s^{-1}) with a relaxation rate similar to the value observed for $JunC^{SFlu}$ mixed with $FosC^{SRho}$ (0.55 s^{-1}), indicating that the rate of dimerization is relatively unaffected by removal of the basic region (see Table 3). However, in the presence of calf thymus DNA, the fluorescence decrease observed for $JunLZ^{SFlu}$ mixed with $FosC^{SRho}$ is still fit by a single exponential and the rate is the same as that observed in the absence of DNA (0.61 or 0.47 s^{-1} versus 0.40 s^{-1}; see also Table 3).

Another control was performed to verify that the increased rate of fluorescence quenching results from dimerization occurring on DNA polymers and is not the result of an increased rate of hydrophobic collapse due to negative charge on the DNA (*50*). In this experiment, 20 nM $JunC^{SFlu}$ was mixed with 100 nM $FosC^{SRho}$ and either no nucleic acid, 1 μM dNTPs, or 500 nM bp calf thymus DNA. As observed previously, the addition of calf thymus DNA increased the rate of fluorescence quenching (Figure 8D, Table 3). In the absence of DNA, the rate was monophasic; whereas addition of 500 nM bp calf thymus DNA changed the relaxation to a biphasic decay. Addition of 1 μM dNTPs (a nucleotide concentration equivalent to that of 500 nM bp calf thymus DNA) had essentially no effect on the relaxation rate, which was now monophasic with a relaxation rate (0.80 s^{-1}) similar to that observed in the absence of DNA (0.55 s^{-1}, Table 3).

Monomer Binding Models Provide the Best Fit to Experimental Data. Kinetic traces were acquired at 20 different ratios of $FosC^{SRho}$ to $JunC^{SFlu}$ to calf thymus DNA (Table 2). Both the rates and magnitudes of fluorescein quenching depend on the concentrations of all three components. The kinetic data were fit using the computer program Dynafit (*41*) (Figure 9). The Dynafit algorithm first performs a nonlinear least-squares regression to optimize unknown parameters (rate constants and fluorescence responses) in the context of each proposed model. Using the best fit parameters, the different models are then assessed for their ability to model the experimental data. Seven different statistical criteria are used in the assessment, including the summed least-squares residuals. The best fits will be characterized by the smallest summed least-squares value.

The dimer model produced the poorest fit to the data; one reflection of the poor fit is its production of the highest value for the summed least-squares residual (Figure 9B). Statistical analysis indicates that any other model considered is at least 95% more likely to provide the best fit to the data. (See Supporting Information for further statistical comparisons.) Furthermore, the rate constants required to produce even this poor fit were physically unreasonable. For example, although the algorithm correctly identified the association rate of the first step in the dimer binding pathway [$k_{1df} = (4.56 \pm 0.16) \times 10^6$ M^{-1} s^{-1} is close to the value, $(7.36 \pm 0.11) \times 10^6$ M^{-1} s^{-1}, determined in the absence of DNA], the association rate constant determined for the second step ($k_{2df} = 8.20 \times 10^{12}$ M^{-1} s^{-1}) is 3 orders of magnitude faster than that allowed by electrostatically assisted diffusion control (*19*). Finally, the dissociation rate constant determined for the second step of the dimer pathway, dissociation of the Fos·Jun dimer from DNA, was 17 066 s^{-1}. This fast rate constant suggests that the final complex is unstable, in direct contrast to experimental observations (J.J.K., unpublished data and refs *46* and *47*).

Both the Fos binding pathway and the Jun binding pathway provided better fits to the data. Simulations based on these

Table 2: Relaxation Rates and Amplitudes Describing the Quenching of $JunC^{SFlu}$ by $FosC^{SRho}$ in the Absence and Presence of Calf Thymus DNA

[$JunC^{SFlu}$] (nM)	[$FosC^{SRho}$] (nM)	[calf thymus DNA bp] (nM)	τ_1 (s^{-1})	A_1 (arbitrary units)	τ_2 (s^{-1})	A_2 (arbitrary units)
20	50	0	0.36 ± 0.02	0.23 ± 0.01		
20	50	50	0.29 ± 0.08	0.11 ± 0.02	1.5 ± 0.4	0.09 ± 0.03
20	50	500	0.36 ± 0.05	0.12 ± 0.01	2.5 ± 0.6	0.07 ± 0.01
20	50	5000	0.38 ± 0.05	0.17 ± 0.02	2.1 ± 0.6	0.10 ± 0.02
20	200	0	1.56 ± 0.02	1.21 ± 0.01		
20	200	50	0.96 ± 0.13	0.49 ± 0.12	2.4 ± 0.3	0.8 ± 0.2
20	200	500	1.04 ± 0.06	0.31 ± 0.02	5.0 ± 0.4	0.37 ± 0.02[a]
20	200	5000	1.15 ± 0.05	0.26 ± 0.01	17.6 ± 2.4	0.18 ± 0.02[a]
50	50	0	0.34 ± 0.01	0.42 ± 0.003		
50	50	50	0.35 ± 0.01	0.36 ± 0.003		
50	50	500	0.37 ± 0.01	0.32 ± 0.003		
50	50	5000	0.33 ± 0.03	0.14 ± 0.003	9.8 ± 2.6	0.07 ± 0.02
50	200	0	1.60 ± 0.02	1.59 ± 0.007		
50	200	50	1.32 ± 0.04	0.76 ± 0.007	6.0 ± 0.4	0.65 ± 0.03
50	200	500	1.03 ± 0.04	0.34 ± 0.008	13.4 ± 0.8	0.47 ± 0.02[a]
50	200	5000	1.19 ± 0.05	0.36 ± 0.01	11.6 ± 0.8	0.44 ± 0.02[a]
100	200	0	1.18 ± 0.01	4.50 ± 0.01		
100	200	50	0.61 ± 0.09	0.80 ± 0.12	2.04 ± 0.05	3.9 ± 0.2
100	200	500	1.94 ± 0.05	1.96 ± 0.03	10.4 ± 0.5	1.21 ± 0.04
100	200	5000	2.61 ± 0.09	0.57 ± 0.01	26.8 ± 0.8	1.47 ± 0.03

[a] In several cases, the amplitude of the fast phase appears to decrease with increasing DNA concentration. In these cases the rate of the fast phase is increased dramatically and we believe that the extremely fast rate causes us to fail to observe the earliest time points (see the Supporting Information for the data). This artifact may cause an underestimate of the rate of dimer formation.

Table 3: Relaxation Rates and Amplitudes for Control Experiments. $FosC^{SRho}$ Quenching of Various Fluorescence Donors in the Presence and Absence of Nucleic Acid Components

fluorescence donor[a]	nucleic acid	τ_1 (s^{-1})	A_1[b]
20 nM $JunC^{SFlu}$	none	0.55 ± 0.01	0.88 ± 0.01
20 nM $JunC^{SFlu}$	500 nM CT DNA[c]	0.90 ± 0.09[d]	0.48 ± 0.01[d]
20 nM $JunC^{SFlu}$	1 μM dNTPs	0.80 ± 0.02	0.69 ± 0.01
20 nM $FosC^{SFlu}$	none	0.43 ± 0.09	0.13 ± 0.01
20 nM $FosC^{SFlu}$	200 nM CT DNA[c]	0.28 ± 0.04	0.17 ± 0.02
20 nM $JunLZ^{SFlu}$	none	0.47 ± 0.02	1.00 ± 0.01
20 nM $JunLZ^{SFlu}$	200 nM CT DNA[c]	0.61 ± 0.02	0.67 ± 0.01
20 nM $JunLZ^{SFlu}$	2 μM CT DNA[c]	0.40 ± 0.01	0.91 ± 0.01

[a] 100 nM $FosC^{SRho}$ served as the fluorescence acceptor in all experiments. [b] Amplitudes (A_1 and A_2) are the magnitudes of fluorescence change given in arbitrary units. [c] CT DNA is calf thymus DNA, concentrations indicated are per base pair. [d] Mixing 20 nM $JunC^{SFlu}$ with 100 nM $FosC^{SRho}$ and 500 nM CT DNA results in a kinetic trace best fit by a double exponential with $\tau_2 = 3.8 \pm 0.2\ s^{-1}$ and $A_2 = 0.70 \pm 0.03$.

models included the first, but not the second, step in the dimer binding pathway. These models assume that all DNA binding occurs through a monomer pathway, but that $FosC^{SRho}$ and $JunC^{SFlu}$ can still dimerize as they do in the absence of DNA. Both models optimized the parameter k_{d1f} to values similar to that determined in the absence of DNA: $k_{1df} = (14.9 \pm 0.8) \times 10^6\ M^{-1}\ s^{-1}$ for the Fos model and $k_{1df} = (15.5 \pm 0.7) \times 10^6\ M^{-1}\ s^{-1}$ for the Jun model. The association rate constants for both steps in both pathways were physically reasonable, the fastest being the second step in the Fos pathway, $k_{f2f} = 34.4 \times 10^6\ M^{-1}\ s^{-1}$.

The inclusion of the dimer pathway did not improve the fit of either the Fos or Jun model, despite increasing the number of optimizable parameters (Figure 9B). Furthermore, the optimized association rate constant for the second step in the dimer pathway ($k_{d2f} = 10\ M^{-1}\ s^{-1}$ in both cases) was smaller than any monomer pathway association rate constant, indicating that flux through the dimer pathway is a minor contributor to overall reaction velocity in these simulations.

Considering the Fos and Jun binding pathways together resulted in a fit improved over either alone. This model accurately determined the rate constant for the first step in the dimer pathway [$k_{d1f} = (13.7 \pm 0.8) \times 10^6\ M^{-1}\ s^{-1}$] and produced physically reasonable association rate constants for both steps in both the Fos and Jun binding pathways. Furthermore, the dissociation rate constants determined for the final steps in the Fos and Jun binding pathways were both less than 1 s^{-1}, consistent with the observed stability of the final complex.

Addition of the dimer pathway to the joint simulation of the Fos and Jun pathways did not improve the fit. The association rate constant for the second step in the dimer pathway (k_{d2f}) was optimized to 10 $M^{-1}\ s^{-1}$, indicating that when all three pathways are considered together, the dimer pathway contributes little to the overall reaction rate.

DISCUSSION

FRET Can Be Used To Study Fos·Jun Dimerization. The use of the fluorescein-tetramethylrhodamine FRET system provides a convenient means to measure dimerization kinetics of bZIP element peptides. Quenching of fluorescein emission was shown to be an accurate measure of Fos·Jun dimer formation, either on or off of DNA. This system provided a means to evaluate the rate and extent of dimer formation in solution and independent of DNA binding. Since the fluorescence acceptor, $FosC^{SRho}$, does not homodimerize appreciably ($K_d \approx 6\ \mu M$), its concentration could be varied up to 500 nM to allow for accurate determination of equilibrium dissociation constants and association rate constants.

The dissociation constant we determined to describe the equilibrium between monomeric and dimeric forms of our fluorescein-modified Jun peptide (4.7 μM) is similar to the value measured by Daugherty and Gellman for an unmodified Jun leucine zipper (6.5 μM). Daugherty and Gellman observed higher order aggregation for fluorescently modified

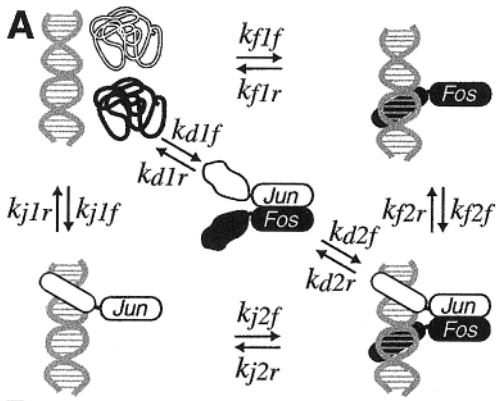

B

Model	k_{d1f} k_{d1r}	k_{d2f} k_{d2r}	k_{f1f} k_{f1r}	k_{f2f} k_{f2r}	k_{j1f} k_{j1r}	k_{j2f} k_{j2r}	Parameters	Sum of Squares
Dimer	●	●					4	0.0861
Fos	●		●	●			6	0.0818
Jun	●				●	●	6	0.0778
Dimer + Fos	●	●	●	●			7	0.0819
Dimer + Jun	●	●			●	●	7	0.0778
Fos + Jun	●		●	●	●	●	9	0.0766
Dimer + Fos + Jun	●	●	●	●	●	●	10	0.0766

FIGURE 9: (A) Three different pathways could describe the formation of a Fos·Jun·DNA complex. Each pathway consists of two steps where each step is described by a forward and a reverse rate constant. In the dimer pathway (diagonal equilibria) Fos and Jun first dimerize and then bind DNA. In the Jun pathway (left and bottom equilibria) the Jun monomer binds DNA and then recruits the Fos monomer. In the Fos pathway (top and right equilibria) the Fos monomer binds DNA, followed by binding of the Jun monomer. (B) Seven models of DNA binding were simulated using the Dynafit algorithm (*41*). The models include the dimer binding pathway, the Jun binding pathway, the Fos binding pathway and combinations thereof. The filled circles show the rate constants that were optimized for each model. Parameters are the number of optimized values in each simulation and include rate constants and fluorescence responses. Sums of squares are the summed least squares residuals for each simulation. The Dynafit algorithm chose the model comprised of the Fos and Jun monomer binding pathways as the best-fit model based on seven statistical criteria.

versions of the Jun leucine zipper (*48*). We do not observe such behavior, perhaps because our constructs include a highly charged basic segment that should inhibit aggregation, or because they carry the fluorophore at the C-terminus of the leucine zipper, or because our stopped-flow experiments were conducted at low peptide concentrations that disfavor aggregation.

Fos and Jun Dimerize Rapidly in the Absence of DNA. Stopped-flow fluorescence measurements were used to assess the rate of $FosC^{SRho}$·$JunC^{SFlu}$ dimer formation. Kinetic traces were subjected to a global fit according to a two-state model to determine the rate constants [$k_{1df} = (7.36 \pm 0.11) \times 10^6$ M^{-1} s^{-1} and $k_{1dr} = 0.064 \pm 0.003$ s^{-1}] describing the monomer−dimer equilbrium. The K_d calculated from these rate constants was 8.7 nM, a factor of 6 less than the value determined by equilibrium FRET and similar to reported values (*49*, *50*).

Previous kinetic studies of the dimerization properties of bZIP proteins have focused on the leucine zipper of GCN4 and on homodimeric model leucine zipper peptides. For such peptides, association rates range from 8×10^4 M^{-1} s^{-1} to 3×10^8 M^{-1} s^{-1} (*40*, *51*−*56*). The Fos and Jun peptides studied here preferentially form heterodimers due to the net negative charge (−5) of the Fos leucine zipper and the net positive charge (+2) of the Jun leucine zipper. As such, they are most similar to a model heterodimeric leucine zipper formed from oppositely charged monomers. At similar ionic strength (144 mM), rate constants describing the monomer−dimer equilibrium of heterodimeric model peptides, $k_f = (25.7 \pm 3) \times 10^6$ M^{-1} s^{-1} and $k_r = 0.217 \pm 0.4$ s^{-1} (*57*), were comparable to those found here.

DNA Enhances the Rate of Dimer Formation. The DNA binding kinetics of bZIP proteins have been studied less frequently than their dimerization kinetics (*16*, *49*, *58*). Stopped-flow fluorescence studies conducted using GCN4 monomers and dimers showed that both bound DNA at a diffusion-controlled rate and allowed the authors to infer that DNA binding occurred through the monomer pathway (*16*). The rapid binding combined with the relatively high concentrations of peptide and DNA used in the GCN4 experiments precluded quantitative determination of the DNA binding rate.

In the experiments described here, the presence of DNA results in increases in the rate and magnitude of fluorescein emission quenching upon mixing of $FosC^{SRho}$ and $JunC^{SFlu}$. We interpret these changes to be indicative of increases in the rate and amount of $FosC^{SRho}$·$JunC^{SFlu}$ dimer formation. The increased rate of dimerization observed in the presence of calf thymus DNA is not merely a result of the increased anionic strength of the reaction mixture: when a Jun peptide lacking a basic region was used, DNA had no effect on the rate of dimerization. Dimerization at an increased rate appears to require DNA binding by the peptides, suggesting a monomer pathway for DNA binding.

Dimer Pathway is Both Inadequate and Unnecessary To Describe DNA Binding. Simulations show that pathways in which the first step comprises binding of a bZIP monomer to DNA provide the best fit to experimental data. To fit the experimental data, the dimer DNA binding pathway would require an association rate constant of 10^{12} M^{-1} s^{-1} for formation of the dimer·DNA complex, a number which is physically unreasonable. Invoking the dimer binding pathway along with one or more monomer binding pathways does not improve the fit to the data despite increasing the number of parameters. We propose that Fos and Jun bind DNA by a combination of pathways in which Jun and Fos each bind DNA individually and then recruit the second binding partner.

This work provides an additional example of the growing number of dimeric DNA-binding proteins that have been shown to form complexes with DNA via a monomer pathway. These proteins include members of the bZIP (*15*, *16*, *59*), bHLH (*60*), bHLHZip (*17*), and nuclear hormone receptor (*6*) families as well as the LexA (*14*) and Arc (*20*) repressors. Recently, the tetrameric GA-binding protein has been shown to bind DNA by an analogous stepwise pathway, in which a single $\alpha-\beta$ heterodimer binds DNA, followed by binding of a second heterodimer (*61*). The monomer pathway appears to be a general mechanism for binding,

which allows faster and more specific formation of the final complex (*17*, *21*, *23*). In this case, we show that even a protein with a thermodynamically stable dimerization interface (K_d = 54 nM) does not need to form a dimer before binding DNA.

Two Monomer Pathways Provide the Best Fit to the Data. Simulations of the two monomer binding pathways, Jun binding first and Fos binding first, show that both provide a better fit to the experimental data than the dimer binding pathway. Furthermore, a simulation using a combination of the two monomer binding pathways provides a better fit to the data than the simulation of either pathway alone. It seems likely that both monomer pathways contribute to DNA binding; however, it is formally possible that only the Fos or the Jun pathway is operative. The Jun peptide used here has a net charge of +13 while the Fos peptide has a charge of +6, hinting that the Jun peptide might experience a stronger electrostatic driving force for DNA binding.

The simulation that invokes both the Fos and Jun monomer binding pathways produces rate constants that predict that the Jun monomer will recognize DNA with an affinity of 638 nM and the Fos monomer will have an affinity of 628 nM for DNA. The simulated rate constants also predict that the complexes will dissociate at rates of 0.16 and 0.59 s^{-1}, respectively. The rate constants correspond to half-lives of 2.5 s for the Jun monomer·DNA complex and 1.2 s for the Fos monomer·DNA complex. In a biological context, the total amount of monomer·DNA complex at any time will depend on the concentrations of accessible DNA and of each protein.

bZIP monomer·DNA complexes are not generally observed, particularly in gel electrophoresis experiments where the observation of kinetically unstable species is difficult. The conditions used in the gel electrophoresis experiments described here use equimolar quantities of Fos and Jun and with the total protein concentration in at least 10-fold excess of DNA concentration. Such conditions will not favor formation of monomer·DNA complexes, and the primary protein·DNA species is the dimer·DNA complex. However, in the stopped-flow fluorescence experiments described here, DNA is in large excess, and the effects of mass action would be expected to drive formation of monomer·DNA complexes (*62*). Removing the stabilizing effect of the leucine zipper dimerization region can also promote observation of the monomer·DNA complex. Complexes formed from bZIP basic region monomers and DNA have been observed [T. L. Schneider and A. Schepartz, unpublished observations and (*15*, *18*, *63*)]. The predicted thermodynamic stabilities of the monomer·DNA complexes based on our simulations (638 and 628 nM) are similar to the estimate of 1 μM made by others (*18*, *64*).

Low levels of cJun are found in many cell types (*25*). Like cFos, though, cJun has an important role as an inducible transcription factor, and many of the same stimuli (serum, EGF, TNF-α, UV) contribute to the induction of cFos and cJun (*24*−*27*). Rapid induction of cFos and cJun may lead to rapid DNA binding by the monomers, followed by recruitment of the binding partner to produce a stable complex. It is important to note, however, that the peptides used here are only small fragments of the full-length proteins. In the context of the full-length proteins, other domains may affect the monomer−dimer equilibrium and thereby alter the preferred DNA binding pathway.

Influence of Other Proteins. The experiments shown here address the assembly of Fos·Jun·DNA complexes in vitro. Assembly of these complexes in vivo will be subject to additional variables, such as high concentrations of nonspecific nucleic acid, much of it packaged in chromatin, competition with other DNA-binding proteins and interactions with the transcriptional machinery. In particular, the Fos·Jun dimer is known to bind cooperatively with a Rel homology protein, nuclear factor of activated T-cells (NFAT), to ARRE-containing DNA (*65*, *66*). NFAT's target site is found in the ARRE site, adjacent to a nonconsensus AP-1 target site. Binding of either NFAT or AP-1 alone to the ARRE site is low affinity; however, they bind cooperatively to form a stable complex [for reviews of NFAT function see (*67*, *68*)].

The cocrystal structure of the Fos·Jun·NFAT·DNA complex shows that NFAT contacts both Fos and Jun as well as binding to DNA (*69*). One possible explanation for the NFAT-induced enhancement in AP-1 binding is that NFAT shifts the Fos·Jun equilibrium to favor dimers. However, NFAT does not appear to have an effect on the dimerization of Fos and Jun in the absence of DNA (J.J.K., unpublished data and ref *70*). Yeast one-hybrid experiments have shown that mutation of a single conserved residue in Jun (R286) abolishes the cooperative binding between AP-1 and NFAT (*66*). No such effect was observed for any residue in Fos. A possible assembly mechanism consistent with these data is the one in which AP-1 binds DNA by a monomer pathway and in which NFAT stabilizes both an intermediate in the monomer pathway, the Jun·DNA species, as well as the final AP-1·DNA complex.

ACKNOWLEDGMENT

We thank Lin Chen and Steve Harrison for supplying the clones used to generate all Fos and Jun expression vectors and Stacey Rutledge and Luke Rice for comments on the manuscript.

SUPPORTING INFORMATION AVAILABLE

Kinetic traces used to extract the data presented in Table 2 and the statistical differences between the fits produced by the seven different DNA binding models. This material is available free of charge via the Internet at http://pubs.acs.org.

REFERENCES

1. Gill, G. (1994) *Curr. Biol. 4*, 374−376.
2. Roeder, R. G. (1996) *Trends Biochem. Sci. 21*, 327−334.
3. Choy, B., Roberts, S. G. E., Griffin, L. A., and Green, M. R. (1993) *Cold Spring Harbor Symp. Quant. Biol. 58*, 199−203.
4. Choy, B., and Green, M. R. (1993) *Nature 366*, 531−536.
5. Li, X.-Y., Virbasius, A., Zhu, X., and Green, M. R. (1999) *Nature 399*, 605−609.
6. Holmbeck, S. M. A., Dyson, H. J., and Wright, P. E. (1998) *J. Mol. Biol. 284*, 533−539.
7. Shuai, K., Horvath, C. M., Huang, L. H. T., Qureshi, S. A., Cowburn, D., and Darnell, J. E., Jr. (1994) *Cell 76*, 821−828.
8. Hurst, H. C. (1994) *Protein Profile 1*, 123−168.
9. Wolberger, C. (1996) *Curr. Opin. Struct. Biol. 6*, 62−68.

10. May, M. J., and Ghosh, S. (1997) *Semin. Cancer Biol. 8*, 63−73.
11. Littlewood, T. D., and Evan, G. I. (1994) *Protein Profile 1*, 639−709.
12. Foley, K. P., and Eisenman, R. N. (1999) *Biochim. Biophys. Acta 1423*, M37-M47.
13. Solomon, D. L. C., Amati, B., and Land, H. (1993) *Nucleic Acids Res. 21*, 5372−5376.
14. Kim, B., and Little, J. W. (1992) *Science 255*, 203−206.
15. Metallo, S. J., and Schepartz, A. (1997) *Nat. Struct. Biol. 4*, 115−117.
16. Berger, C., Piubelli, L., Haditsch, U., and Bosshard, H. R. (1998) *FEBS Lett. 425*, 14−18.
17. Kohler, J. J., Metallo, S. J., Schneider, T. L., and Schepartz, A. (1999) *Proc. Natl. Acad. Sci. U.S.A. 96*, 11735−11739.
18. Park, C., Campbell, J. L., and Goddard, W. A., III (1996) *J. Am. Chem. Soc. 118*, 4235−4239.
19. Schreiber, G., and Fersht, A. R. (1996) *Nat. Struct. Biol. 3*, 427−431.
20. Rentzeperis, D., Jonsson, T., and Sauer, R. T. (1999) *Nat. Struct. Biol. 6*, 569−573.
21. Shoemaker, B. A., Portman, J. J., and Wolynes, P. G. (2000) *Proc. Natl. Acad. Sci. U.S.A. 97*, 8868−8873.
22. Rastinejad, F., Perlmann, T., Evans, R. E., and Sigler, P. B. (1995) *Nature 375*, 203−211.
23. Pomerantz, J. L., Wolfe, S. A., and Pabo, C. O. (1998) *Biochemistry 37*, 965−970.
24. Herdegen, T., and Leah, J. D. (1998) *Brain Res. Rev. 28*, 370−490.
25. Karin, M., Liu, Z. G., and Zandi, E. (1997) *Curr. Opin. Cell Biol. 9*, 240−246.
26. Karin, M. (1995) *J. Biol. Chem. 270*, 16483−16486.
27. Angel, P., and Karin, M. (1991) *Biochim. Biophys. Acta 1072*, 129−157.
28. Bohmann, D., Bos, T. J., Admon, A., Nishimura, T., Vogt, P. K., and Tjian, R. (1987) *Science 238*, 1386−1392.
29. Vanstraaten, F., Muller, R., Curran, T., Vanbeveren, C., and Verma, I. M. (1983) *Proc. Natl. Acad. Sci. U.S.A. 80*, 3183−3187.
30. Abate, C., Patel, L., Rauscher, F. J., III, and Curran, T. (1990) *Science 249*, 1157−1161.
31. Stryer, L. (1978) *Annu. Rev. Biochem. 47*, 819−846.
32. Lakowicz, J. R. (1983) *Principles of Fluorescence Spectroscopy*, Plenum Press, Plenum Press.
33. Epps, D. E., Poorman, R., Hui, J., Carlson, W., and Heinrikson, J. (1987) *J. Biol. Chem. 262*, 10570−10573.
34. Demas, J. N., and Crosby, G. A. (1971) *J. Phys. Chem. 75*, 991−1024.
35. Eis, P. S., and Millar, D. P. (1993) *Biochemistry 32*, 13852−13860.
36. Parkhurst, K. M., Brenowitz, M., and Parkhurst, L. J. (1996) *Biochemistry 35*, 7459−7465.
37. Perkins, T. A., Wolf, D. E., and Goodchild, J. (1996) *Biochemistry 35*, 16370−16377.
38. Lacourciere, K. A., Stivers, J. T., and Marino, J. P. (2000) *Biochemistry 39*, 5630−5641.
39. Cantor, C. R., and Schimmel, P. R. (1980) *Biophys. Chem.*, Freeman, New York.
40. Zitzewitz, J. A., Bilsel, O., Luo, J., Jones, B. E., and Matthews, C. R. (1995) *Biochemistry 34*, 12812−12819.
41. Kuzmic, P. (1996) *Anal. Biochem. 237*, 260−273.
42. Metallo, S. J., and Schepartz, A. (1994) *Chem. Biol. 1*, 143−151.
43. Glover, J. N. M., and Harrison, S. C. (1995) *Nature 373*, 257−261.
44. Furey, W. S., Joyce, C. M., Osborne, M. A., Klenerman, D., Peliska, J. A., and Balasubramanian, S. (1998) *Biochemistry 37*, 2979−1990.
45. O'Shea, E. K., Rutkowski, R., Stafford, W. F., III., and Kim, P. S. (1989) *Science 245*, 646−648.
46. Cohen, D. R., and Curran, T. (1990) *Oncogene 5*, 929−939.
47. Rauscher, F. J., Voulalas, P. J., Franza, B. R., and Curran, T. (1988) *Genes Dev. 2*, 1687−1699.
48. Daugherty, D. L., and Gellman, S. H. (1999) *J. Am. Chem. Soc. 121*, 4325−4333.
49. Patel, L. R., Curran, T., and Kerppola, T. K. (1994) *Proc. Natl. Acad. Sci. U.S.A. 91*, 7360−7364.
50. Pernelle, C., Clerc, F. F., Dureuil, C., Bracco, L., and Tocque, B. (1993) *Biochemistry 32*, 11682−11687.
51. Jelesarov, I., Durr, E., Thomas, R. M., and Bosshard, H. R. (1998) *Biochemistry 37*, 7539−7550.
52. Wendt, H., Baici, A., and Bosshard, H. R. (1994) *J. Am. Chem. Soc. 116*, 6973−6974.
53. Sosnick, T. R., Jackson, S., Wilk, R. R., Englander, S. W., and DeGrado, W. F. (1996) *Proteins 24*, 427−432.
54. Zitzewitz, J. A., Ibarra-Molero, B., Fishel, D. R., Terry, K. L., and Matthews, C. R. (2000) *J. Mol. Biol. 296*, 1105−1116.
55. Durr, E., Jelesarov, I., and Bosshard, H. R. (1999) *Biochemistry 38*, 870−880.
56. Wendt, H., Berger, C., Baici, A., Thomas, R. M., and Bosshard, H. R. (1995) *Biochemistry 34*, 4097−4107.
57. Wendt, H., Leder, L., Harma, H., Jelesarov, I., Baici, A., and Bosshard, H. R. (1997) *Biochemistry 36*, 204−213.
58. Okahata, Y., Niikura, K., Sugiura, Y., Sawada, M., and Morii, T. (1998) *Biochemistry 37*, 5666−5672.
59. Wu, X. L., Spiro, C., Owen, W. G., and McMurray, C. T. (1998) *J. Biol. Chem. 273*, 20820−20827.
60. Wendt, H., Thomas, R. M., and Ellenberger, T. (1998) *J. Biol. Chem. 273*, 5735−5743.
61. Chinenov, Y., Henzl, M., and Martin, M. E. (2000) *J. Biol. Chem. 275*, 7749−7756.
62. Bray, D., and Lay S. (1997) *Proc. Natl. Acad. Sci. U.S.A. 94*, 13493−13498.
63. Zondlo, N. J., and Schepartz A. (1999) *J. Am. Chem. Soc. 121*, 6938−6939.
64. Blackwell, T. K., Bowerman, B., Priess, J. R., and Weintraub, H. (1994) *Science 266*, 621−628.
65. McCaffrey, P. G., Luo, C., Kerppola, T. K., Jain, J., Badalian, T. M., Ho, A. M., Burgeon, E., Lane, W. S., Lambert, J. N., Curran, T., Verdine, G. L., Rao, A., and Hogan, P. (1993) *Science 262*, 750−752.
66. Peterson, B. R., Sun, L. J., and Verdine, G. L. (1996) *Proc. Natl. Acad. Sci. U.S.A. 93*, 13671−13676.
67. Masuda, E. S., Imamura, R., Amasaki, Y., Arai, K., and Arai, N. (1998) *Cell. Signal. 10*, 599−611.
68. Rao, A., Luo, C., and Hogan, P. G. (1997) *Annu. Rev. Immunol. 15*, 707−747.
69. Chen, L., Glover, J. N. M., Hogan, P. G., Rao, A., and Harrison, S. C. (1998) *Nature 392*, 42−48.
70. Chen, L., Oakley, M. G., Glover, J. N. M., Jain, J., Dervan, P. B., Hogan, P. G., Rao, A., and Verdine, G. L. (1995) *Curr. Biol. 5*, 882−889.

BI001881P